

Article

# Current Harmonic Suppression Algorithm for Asymmetric Dual Three-Phase PMSM

Zhihong Wu <sup>1,2</sup>, Weisong Gu <sup>1</sup>, Ke Lu <sup>1,2,\*</sup>, Yuan Zhu <sup>1,2</sup> and Jianbin Guan <sup>2</sup>

<sup>1</sup> School of Automotive Studies, Tongji University, Shanghai 201800, China; zhihong.wu@tongji.edu.cn (Z.W.); AutomotiveGu@163.com (W.G.); yuan.zhu@tongji.edu.cn (Y.Z.)

<sup>2</sup> Sino-German School for postgraduate studies, Tongji University, Shanghai 201800, China; 1731377@tongji.edu.cn

\* Correspondence: luke@tongji.edu.cn; Tel.: +86-13661978920

Received: 1 January 2020; Accepted: 28 January 2020; Published: 2 February 2020



**Abstract:** Based on the vector space decomposition (VSD) transformation, the currents of an asymmetric dual three-phase permanent magnet synchronous motor (ADT-PMSM) with isolated neutral points are decoupled into the torque, producing  $\alpha$ - $\beta$  components in the fundamental subspace and the loss-producing  $x$ - $y$  components in the harmonic subspace. In order to suppress the current harmonics, a feedforward voltage compensation that is calculated according to the dead time, turn on/off time, and the voltage drop is added to the reference voltage of the control algorithm. Due to the limitations of the feedforward voltage compensation method, a feedback current control loop is set up in the  $x$ - $y$  subspace, where an improved resonant controller is adopted to generate the compensation voltage. The improved resonant controller can achieve a high gain at a specific frequency. The experimental results verify the effectiveness of the proposed method.

**Keywords:** asymmetric dual three-phase permanent magnet synchronous motor; vector space decomposition; current harmonic suppression; feedforward voltage compensation; resonant controller

## 1. Introduction

With the wide application of power electronic converters, the motor drive system is no longer limited by the phase number of a traditional three-phase power supply, and the multi-phase motor drive system has been widely concerned [1–5]. The six-phase motor has attracted more and more attention because of its close connection with the traditional three-phase motor. The asymmetric dual three-phase permanent magnet synchronous motor has greater advantages because of smaller torque ripples [5,6]. It has two sets of three-phase windings with isolated neutral points, which are spatially shifted by 30 degrees, as shown in Figure 1.

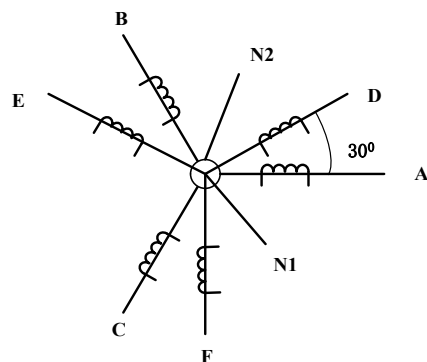


**Figure 1.** Two sets of three-phase windings.

The vector space decomposition (VSD) method is widely adopted for the control of an asymmetric dual three-phase permanent magnet synchronous motor (ADT-PMSM) [7,8]. According to the dimensions of current control, the control methods based on the VSD can be divided into two kinds: two-dimension current control [9,10] and four-dimension current control [11–13]. Two-dimension current control only establishes the current closed-loop control strategy in the  $\alpha$ - $\beta$  subspace where electromechanical energy conversion takes place, while an open-loop control strategy is adopted in the  $x$ - $y$  subspace. The fifth and seventh harmonic voltages due to the dead time effects of inverter will cause large harmonic currents. So, the two-dimension current control cannot achieve the desired results, while the four-dimension current control can control the currents of two subspaces separately. A current closed-loop control strategy is set up in the  $x$ - $y$  subspace to make the harmonic currents 0, which can compensate for the dead-time effects and the nonlinearities of the inverter [13].

In References [14,15], by suitably selecting the voltage vectors from the divided vector groups into one sampling period, the current harmonics can be reduced compared to the Switching Table based Direct Torque Control (ST-DTC) drive. However, this method can only avoid injecting harmonic voltages into the  $x$ - $y$  subspace. However, the dead time and nonlinearities of the inverter are not considered. Methods based on a proportional-integral (PI) controller due to its simple structure and well-known characteristics are employed in the  $x$ - $y$  subspace. However, the fifth and seventh current harmonics are only suppressed to some extent due to its limited bandwidth [16]. Accordingly, a multiple synchronous frame (MSF) scheme based on a PI controller in several synchronous frames (SF) in parallel (one per harmonic) is employed to eliminate the current harmonics in multi-phase machines, which can attain zero steady-state error at different harmonics. However, the computational burden is heavy. In [13,16,17], a resonant controller is employed in an anti-synchronous frame rotating with the negative sequence fundamental frequency in the  $x$ - $y$  subspace to suppress the current harmonics, but the discretization errors of the poles are not considered.

In the field of current harmonics suppression of three-phase motor drives, extensive research has been conducted. Methods based on voltage-second balance theory classify the causes that distort the voltages. By offline measurement of the dead time, the turn-on/off time, and the nonlinearities including the forward voltage drop of the switching device and voltage drop of freewheeling diode, the compensation voltages can be calculated [18–20]. However, these parameters are varied with the junction temperature of the inverter, motor load, speed, and some other factors. Accordingly, online methods are proposed in [21], but these methods add computational burden to the algorithm and require a lookup table to search for the corresponding parameters under certain operating points. Besides, these above-mentioned schemes need the accurate polarities of phase currents [18–21]. Most methods detect the current polarities with current sensors, which are easily polluted by the noises and harmonics. In Reference [22], a specific hardware circuit is designed to detect which antiparallel diode conducts in a one switching cycle to judge the current polarity. However, it adds burden to design the hardware. Similar to the current harmonics suppression of the ADT-PMSM, the resonant controller or the PI controller in the synchronous frames is also adopted [23–26]. Another approach that utilizes the integral term of the d-axis current as feedback to obtain the voltage distortion can only be used on condition that the d-axis reference current is a constant value [27]. Some methods adopt a disturbance observer to estimate the voltage error, which does not need current polarities and the specifications of the inverter [28–31]. However, these methods require lots of efforts to obtain the observer gains and need to have a good knowledge of the motor parameters.

This paper proposes a method that combines the feedforward voltage compensation and the feedback voltage compensation methods together to suppress the current harmonics. The feedforward voltage compensation is obtained by the voltage-second balance theory, and the current detection scheme is independent of current sensors. In order to overcome the problems caused by the junction temperature and some other factors of the inverter, a feedback voltage compensation that employs a resonant controller is put forward. The proposed scheme can achieve the desired results without

additional hardware or a good knowledge of the load parameters. The effectiveness of the proposed method is verified by a set of experimental results.

This paper is structured as follows: Section 2 describes the mathematical model of ADT-PMSM. The analysis of dead-time effects is given in Section 3. The feedforward voltage compensation and feedback current regulator designed in  $x-y$  subspace are discussed in Section 4. Section 5 gives the pulse width modulation (PWM) techniques to implement the four-dimension current control of ADT-PMSM. Experimental results are carried out on an ADT-PMSM experimental platform to verify the effectiveness of the proposed method in Section 6. Finally, the conclusions are summarized in Section 7.

## 2. Machine Model of Asymmetric Dual Three-phase Permanent Magnet Synchronous Motor (ADT-PMSM)

As depicted in Figure 2, the drive system of ADT\_PMSM in this paper has two sets of three-phase voltage source inverters (VSI) sharing the same DC-link voltage, which can supply two sets of three-phase windings.

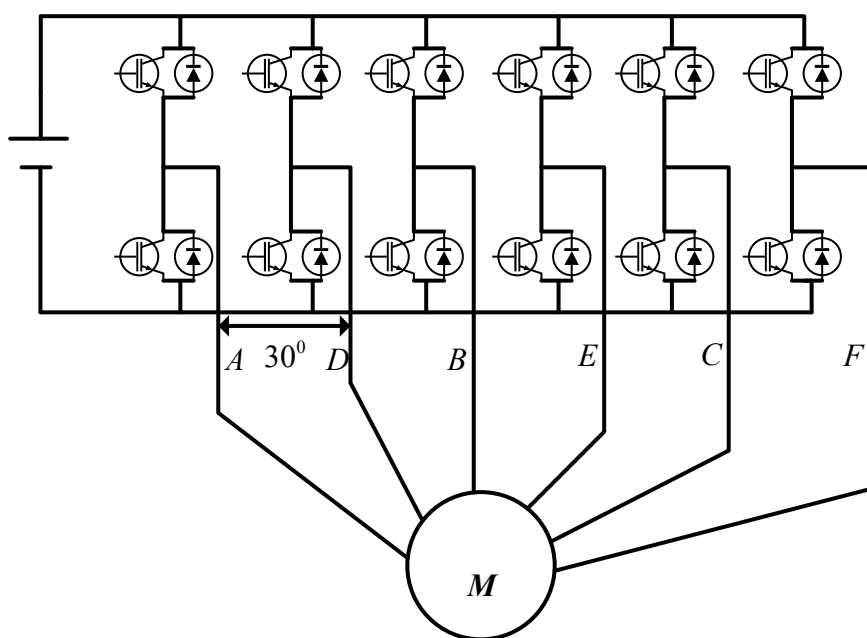


**Figure 2.** Drive system of asymmetric dual three-phase permanent magnet synchronous motor (ADT-PMSM).

According to the VSD theory, the variables including the current, flux, and voltage of the machine can be mapped into three orthogonal subspaces, i.e., the  $\alpha-\beta$ ,  $x-y$ , and zero-sequence subspaces. This approach gives an alternative description of the machine, which is useful for machine control and the development of pulse width modulation (PWM) techniques. Harmonics of different orders are mapped into different subspaces. The fundamental component and harmonics with the order  $12n \pm 1$  ( $n = 1, 2, 3 \dots$ ) are mapped into the  $\alpha-\beta$  subspace. The harmonics with the order  $6n \pm 1$  ( $n = 1, 3, 5 \dots$ ) are mapped into the  $x-y$  subspace. The harmonics with the order  $6n \pm 3$  ( $n = 1, 3, 5 \dots$ ) are mapped into the  $O_1-O_2$  subspace, which is also called the zero sequence subspace. With neutral points being isolated, no current components in the  $O_1-O_2$  subspace would exist. Therefore, the ADT-PMSM with isolated neutrals is a four-order system. The mathematical model and the VSD modeling process of the dual three-phase motor in more detail are introduced in Reference [9]. According to the magnitude invariant principle, the static decoupling transformation matrix is employed as

$$T_{VSD} = \frac{1}{3} \begin{bmatrix} 1 & -\frac{1}{2} & -\frac{1}{2} & \frac{\sqrt{3}}{2} & -\frac{\sqrt{3}}{2} & 0 \\ 0 & -\frac{\sqrt{3}}{2} & \frac{\sqrt{3}}{2} & \frac{1}{2} & \frac{1}{2} & -1 \\ 1 & -\frac{1}{2} & -\frac{1}{2} & -\frac{\sqrt{3}}{2} & \frac{\sqrt{3}}{2} & 0 \\ 0 & -\frac{\sqrt{3}}{2} & \frac{\sqrt{3}}{2} & \frac{1}{2} & \frac{1}{2} & -1 \end{bmatrix}. \quad (1)$$

In order to achieve the vector control, a transformation is used to transform the  $\alpha$ - $\beta$  variables into a synchronous reference frame rotating with the fundamental frequency, i.e.

$$T_{dq} = \begin{bmatrix} \cos \theta & \sin \theta & 0 & 0 & 0 & 0 \\ -\sin \theta & \cos \theta & 0 & 0 & 0 & 0 \\ 0 & 0 & 1 & 0 & 0 & 0 \\ 0 & 0 & 0 & 1 & 0 & 0 \end{bmatrix} \quad (2)$$

where  $\theta$  is the electrical rotor position.

On the condition that the back electromotive force (EMF) is sinusoidal, two sets of windings are symmetric, and mutual leakage inductances are ignored. The voltage equations in the synchronous rotating  $d$ - $q$  coordinate axis in the  $\alpha$ - $\beta$  subspace and in the stationary  $x$ - $y$  coordinate axis in the  $x$ - $y$  subspace are

$$\begin{cases} u_d = i_d R + L_d \frac{di_d}{dt} - w_e L_q i_q \\ u_q = i_q R + L_q \frac{di_q}{dt} + w_e (L_d i_d + \psi_f) \\ u_x = i_x R + L_z \frac{di_x}{dt} \\ u_y = i_y R + L_z \frac{di_y}{dt} \end{cases} \quad (3)$$

where  $R$  is the stator resistance,  $L_d$  and  $L_q$  are the  $d$ - and  $q$ -axes inductances respectively,  $L_z$  is the leakage inductance, and  $u_k(k = d, q, x$  and  $y)$  and  $i_k(k = d, q, x$  and  $y)$  are the voltage and current components, respectively.  $w_e$  is the electrical angular speed, and  $\psi_f$  is the permanent magnet flux.

### 3. Analysis of Dead-Time Effects

In order to facilitate the analysis, Figure 3 shows one phase leg of the widely used six-phase PWM inverter during the dead-time period. If the phase current flows into the stator, the direction is defined as positive and vice versa.

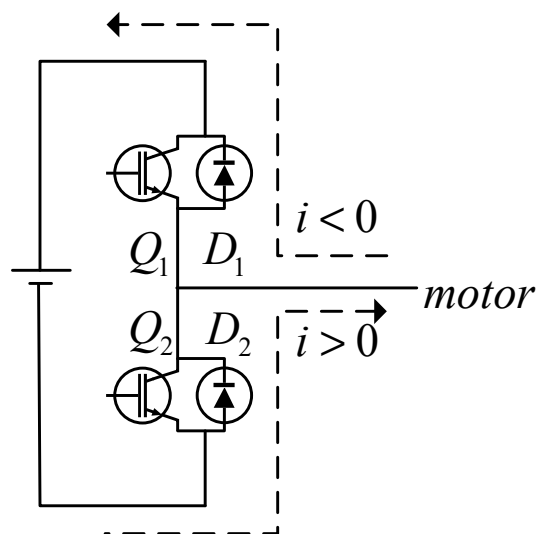


**Figure 3.** Phase leg of the converter during the dead-time period.

In Figure 3, the turn-on time is usually shorter than the turn-off time. In order to avoid the simultaneous conduction of both switching devices Q1 and Q2, fixed dead-time insertion is necessary to ensure the safety of the inverter system. The dead time could cause the desired reference voltages to distort and affect the control performance. During the dead-time period, both switches are turned off, and the current can only flow through the free-wheeling diode D1/D2, if the polarity of phase current is negative/positive. So, the output voltage relies on the direction of phase current during the dead-time period from the above analysis.

Taking the PWM waveforms of one phase leg for example, Figure 4a,b show the situations when the phase current is positive or negative, respectively.

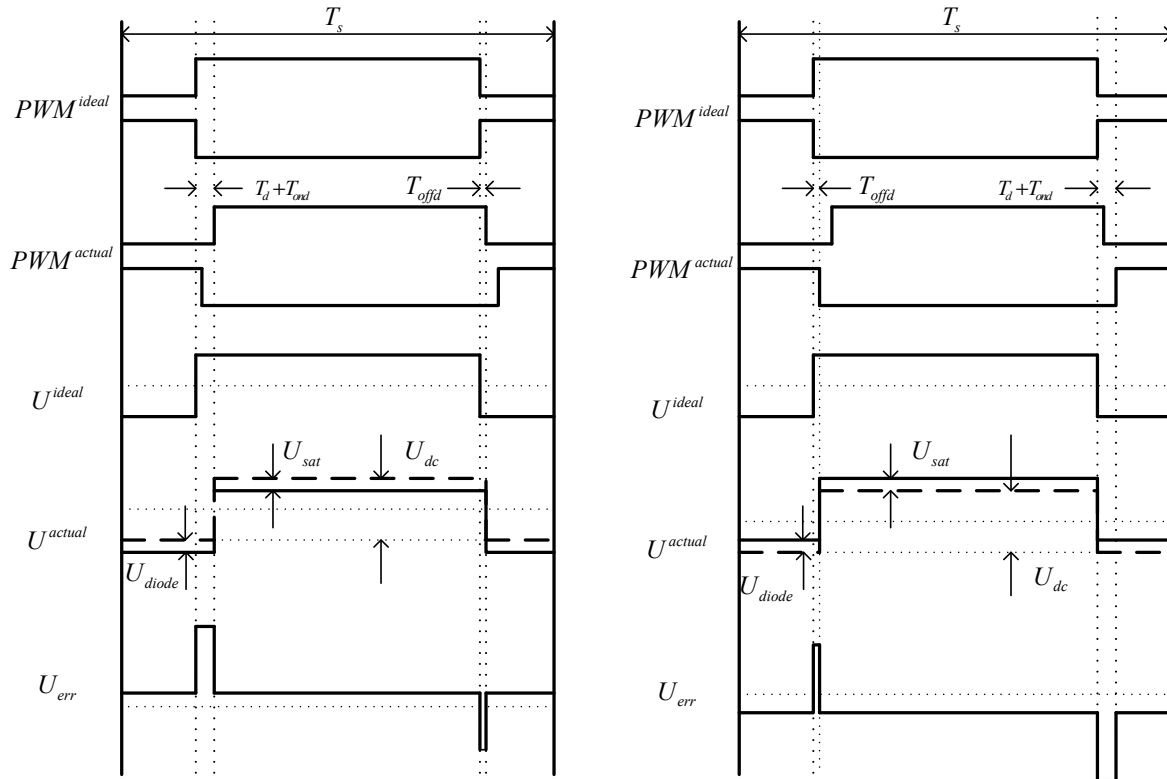


**Figure 4.** Switching patterns and output voltages. (a) Phase current is positive. (b) Phase current is negative.

The average voltage error in one PWM period can be obtained as

$$U_{err} = U_d * sign(i), \quad sign(i) = \begin{cases} -1, & i < 0 \\ 1, & i > 0 \end{cases} \quad (4)$$

where  $sign(x)$  is a sign function and  $U_d$  represents the magnitude of voltage error.  $U_d$  can be expressed as

$$U_d = \frac{T_d + T_{ond} - T_{offd}}{T_s} (U_{dc} - U_{sat} + U_{diode}) + U_v \quad (5)$$

$$U_v = \begin{cases} \frac{T_{on}}{T_s} U_{sat} + \frac{T_{off}}{T_s} U_{diode} & i > 0 \\ \frac{T_{off}}{T_s} U_{sat} + \frac{T_{on}}{T_s} U_{diode} & i < 0 \end{cases} \quad (6)$$

where  $T_d$  is the dead time,  $T_s$  is the PWM carrier period,  $T_{on}$  and  $T_{off}$  are the on-period and off-period of the switching device of the inverter leg, while  $T_{ond}$  and  $T_{offd}$  define the turn-on time delay and turn-off time delay of the switching device, respectively.  $U_{sat}$  and  $U_{diode}$  denote the forward voltage drop of the

switching device and the diode.  $U_v$  represents the average voltage drop in one PWM cycle. The error voltages of six phases can be transformed into the  $x$ - $y$  coordinate axis in the  $x$ - $y$  subspace as follows:

$$\begin{bmatrix} U_{xd} \\ U_{yd} \end{bmatrix} = \frac{1}{3} \begin{bmatrix} 1 & -\frac{1}{2} & -\frac{1}{2} & -\frac{\sqrt{3}}{2} & \frac{\sqrt{3}}{2} & 0 \\ 0 & -\frac{\sqrt{3}}{2} & \frac{\sqrt{3}}{2} & \frac{1}{2} & \frac{1}{2} & -1 \end{bmatrix} \begin{bmatrix} U_{Ad} & U_{Bd} & U_{Cd} & U_{Dd} & U_{Ed} & U_{Fd} \end{bmatrix}^T \quad (7)$$

where  $U_{xd}$  and  $U_{yd}$  are the error voltages in the  $x$ - $y$  coordinate axis in the  $x$ - $y$  subspace, while  $U_{Ad}, U_{Bd}, U_{Cd}, U_{Dd}, U_{Ed}$ , and  $U_{Fd}$  are the error voltages of phase A, B, C, D, E, and F, respectively.

The error voltages in the  $x$ - $y$  subspace can be obtained by applying the Fourier series as follows:

$$\begin{bmatrix} U_{xd} \\ U_{yd} \end{bmatrix} = \frac{4U_d}{\pi} \begin{bmatrix} \sum_{n=6k-1}^{\infty} \frac{\sin n(w_e t + \delta)}{n} + \sum_{n=6k+1}^{\infty} \frac{\sin n(w_e t + \delta)}{n} \\ - \sum_{n=6k-1}^{\infty} \frac{\cos n(w_e t + \delta)}{n} + \sum_{n=6k+1}^{\infty} \frac{\cos n(w_e t + \delta)}{n} \end{bmatrix} \quad k = 1, 3, 5, \dots \quad (8)$$

where  $\delta$  denotes the angle between the current vector  $I_s$  and the  $q$ -axis, as depicted in Figure 5. Here, the anticlockwise rotation is defined as the positive direction. It is noteworthy that the fifth and seventh current harmonics will appear as the +5th and -7th in the  $x$ - $y$  coordinate axis in the  $x$ - $y$  subspace.

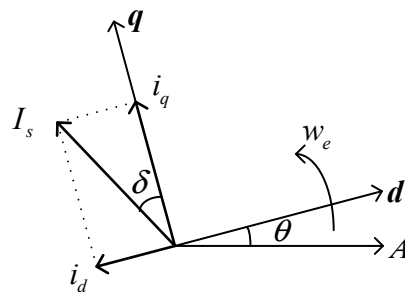


**Figure 5.** Space diagram of current vector angle.

Applying the inverse Park transformation, the error voltages in the anti-synchronous rotating coordinate axis with the negative angular frequency  $+w_e$ , which is defined as the  $x1$ - $y1$  coordinate axis, become

$$\begin{bmatrix} U_{xd}^{x1} \\ U_{yd}^{y1} \end{bmatrix} = \begin{bmatrix} \cos \theta & -\sin \theta \\ \sin \theta & \cos \theta \end{bmatrix} \begin{bmatrix} U_{xd} \\ U_{yd} \end{bmatrix} = \frac{4U_d}{\pi} \begin{bmatrix} \sum_{n=6k}^{\infty} \frac{\sin[n(w_e t + \delta) - \delta]}{n} + \sum_{n=6k}^{\infty} \frac{\sin[n(w_e t + \delta) + \delta]}{n} \\ - \sum_{n=6k}^{\infty} \frac{\cos[n(w_e t + \delta) - \delta]}{n} + \sum_{n=6k}^{\infty} \frac{\cos[n(w_e t + \delta) + \delta]}{n} \end{bmatrix} \quad k = 1, 3, 5, \dots \quad (9)$$

where  $U_{xd}^{x1}$  and  $U_{yd}^{y1}$  are the error voltages in the  $x1$ - and  $y1$ -axes respectively.

After the transformation, it is obvious that the sixth-order voltage components are the main contents of the error voltages. It will influence the motor currents, which will in turn affect the control performance. Assuming that the motor back EMF contains only the fundamental frequency, the sixth-order current harmonics in the virtual anti-synchronous rotating  $x1$ - $y1$  coordinate axis in  $x$ - $y$  subspace are

$$\begin{bmatrix} I_{x1}^6 \\ I_{y1}^6 \end{bmatrix} = \frac{4U_d}{\pi \sqrt{R^2 + (6w_e L_z)^2}} \begin{bmatrix} \frac{\sin(6w_e t + 5\delta - \phi)}{5} + \frac{\sin(6w_e t + 7\delta - \phi)}{7} \\ - \frac{\cos(6w_e t + 5\delta - \phi)}{5} + \frac{\cos(6w_e t + 7\delta - \phi)}{7} \end{bmatrix} \quad (10)$$

where  $\phi = \tan^{-1} \frac{6w_e L_z}{R}$ .

It can be seen that the sixth-order current harmonics are dependent upon the speed and the parameters of the motor.

#### 4. Proposed Current Harmonics Suppression Strategy

##### 4.1. Feedforward Voltage Compensation

The feedforward voltage compensations can be calculated according to Equations (4), (5), and (6) as described in the previous section, so the key issue of the feedforward voltage compensation is to determine the polarities of the phase currents.

This paper proposes a current vector method that uses the current vector angle to judge the polarities of the six-phase currents. The current vector angle that is shown in Figure 5 is defined as follows:

$$\phi = \theta + \text{sign}(i_q) * \pi/2 + \delta \quad (11)$$

Twelve different combinations can be derived according to the polarities of the six-phase currents, which divide the complex plane of the 360-degree electric angle into 12 sectors. Every sector occupies 30 degrees. The corresponding relationship between the current vector angle and the polarities of the six-phase currents are shown in Figure 6.

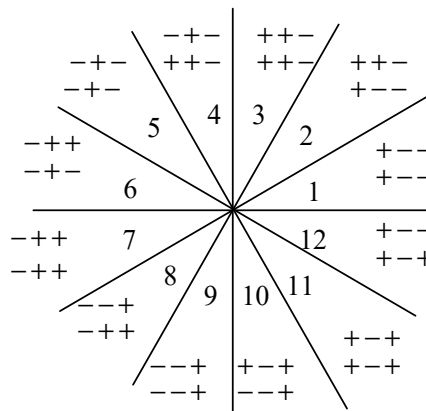


**Figure 6.** Relationship between the current vector angle and polarities of six-phase currents.

So, the polarities of six-phase currents can be defined according to the current vector angle, as shown in Figure 6. Meanwhile, the current vector angle can be calculated according to the current vector in space coordinate, as shown in Equation (11).  $\delta$  can be given as

$$\delta = \text{sign}(i_q) * \arctan \left| \frac{i_d}{i_q} \right| \quad (12)$$

According to Equations (11) and (12), the current vector angle can be obtained as follows:

$$\phi = \theta + \text{sign}(i_q) * (\pi/2 + \arctan \left| \frac{i_d}{i_q} \right|) \quad (13)$$

##### 4.2. Adaptive Feedback Current Control Loop

A feedback current control loop is implemented in the anti-synchronous reference frame to eliminate the sixth-order current harmonics. According to Equation (10), the sixth-order current harmonics in the  $x1-y1$  coordinate axis can be defined as follows:

$$\begin{bmatrix} I_{x1}^6 \\ I_{y1}^6 \end{bmatrix} = \begin{bmatrix} I_{xs} \sin(6w_e t) + I_{xc} \cos(6w_e t) \\ I_{ys} \sin(6w_e t) + I_{yc} \cos(6w_e t) \end{bmatrix} \quad (14)$$

The resonant controller can achieve infinite gain at the specific frequency [16,17,23], which can be expressed in the s-domain as follows:

$$G_R(s) = K_R \frac{s}{s^2 + (hw_e)^2} \quad (15)$$

where  $h$  is the harmonic order, and  $K_R$  is the resonant gain.

When the frequency of ac signal is  $hw_e$ , i.e.,  $s = jhw_e$ , the amplitude can be obtained as

$$|G_R(s)|_{s=jhw_e} = \sqrt{\left(\frac{K_R hw_e}{-w_e^2 + w_e^2}\right)} \quad (16)$$

From Equation (16), it is obvious that the amplitude of  $G_R(s)$  is infinite, which can achieve a zero steady-state error of an AC signal at the resonant frequency. However, the gain of the frequency that is not located at the resonant frequency decreases sharply, which will make the control system more sensitive to the change of input signal frequency and may result in system fluctuation. In addition, due to the limitation of the accuracy of the digital system, the ideal resonant controller is not easy to implement in digital signal processor (DSP). In order to take advantage of the resonant controller, it is necessary to improve the ideal resonant controller. The improved resonant controller can be employed as

$$G_{MR}(s) = \frac{K_R w_c s}{s^2 + 2w_c s + (hw_e)^2} \quad (17)$$

where  $w_c$  is the cut-off frequency.

So, the relationship between output voltage function  $Y(s)$  and current error function  $E(s)$  can be expressed as

$$G_{MR}(s) = \frac{Y(s)}{E(s)} = \frac{K_R w_c s}{s^2 + 2w_c s + (hw_e)^2} \quad (18)$$

which can also be defined as follows:

$$\begin{cases} Y(s) = \frac{1}{s}[K_R w_c E(s) - V_1(s) - V_2(s)] \\ V_1(s) = 2w_c Y(s) \\ V_2(s) = \frac{(hw_e)^2}{s} Y(s) \end{cases} \quad (19)$$

The equivalent schematic block diagram of Equation (19) is shown in Figure 7.

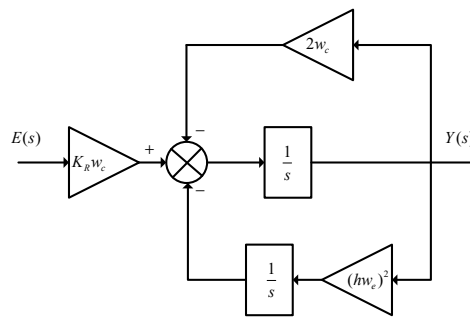


**Figure 7.** Structure of the improved resonant controller.

Figures 8 and 9 show the Bode diagrams of the improved resonant controller. It is obvious that the parameters will influence the system gain and bandwidth. The gain and bandwidth of the improved resonant controller will increase as the parameter  $w_c$  increases, but a large  $w_c$  will affect the frequency selection characteristics of the controller, while the change of  $K_R$  will only influence the gain of the improved resonant controller. It is ideal to choose a larger  $K_R$ , but the stability and convergence will

be affected. So, the best values of  $K_R$  and  $w_c$  should be determined by comprehensive consideration according to the actual situation of the system.

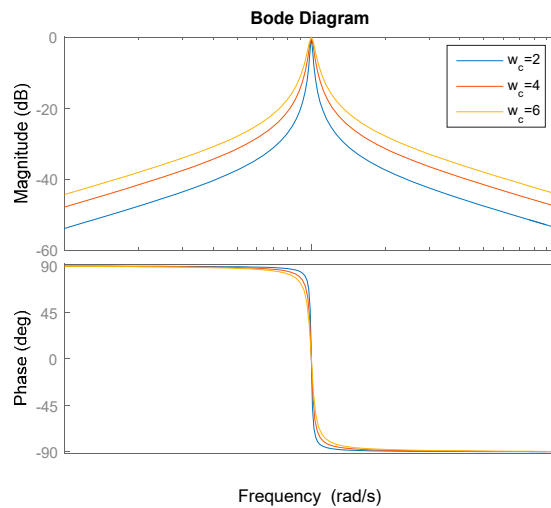


**Figure 8.** Bode diagram for different values of  $w_c$  when  $K_R$  is constant.

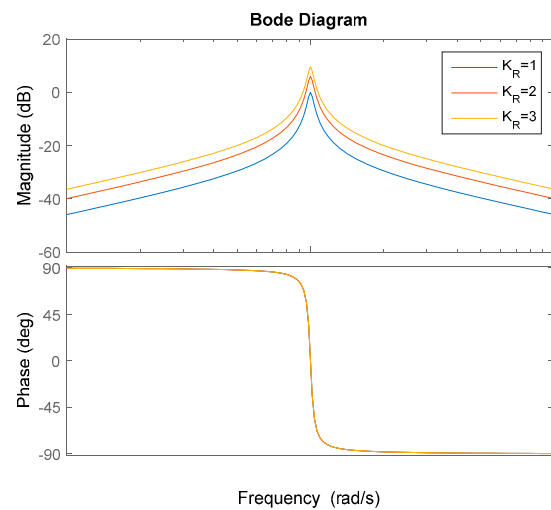


**Figure 9.** Bode diagram for different values  $K_R$  when  $w_c$  is constant.

## 5. Pulse Width Modulation (PWM) Techniques for the Implementation of Four-Dimensional Current Control

The block diagram of four-dimensional current control based on the VSD approach is illustrated in Figure 10, which can compensate for nonlinear factors such as dead-time effects. After the feedback current control loop is adopted in both  $\alpha\beta$  and  $x-y$  subspaces, the desired voltages  $u_\alpha$ ,  $u_\beta$ ,  $u_x$ , and  $u_y$  can be acquired. Applying the inverse VSD transformation, the phase voltages after the feedback current control loop can be obtained as follows:

$$\begin{bmatrix} U_{AN}^* & U_{BN}^* & U_{CN}^* & U_{DN}^* & U_{EN}^* & U_{FN}^* \end{bmatrix}^T = T_{VSD}^{-1} \begin{bmatrix} U_\alpha & U_\beta & U_x & U_y \end{bmatrix}^T \quad (20)$$

Adding the feedforward voltage compensations to the phase voltages obtained from Equation (20), the desired reference phase voltage vector is

$$\begin{bmatrix} U_{AN} & U_{BN} & U_{CN} & U_{DN} & U_{EN} & U_{FN} \end{bmatrix}^T = \begin{bmatrix} U_{AN}^* & U_{BN}^* & U_{CN}^* & U_{DN}^* & U_{EN}^* & U_{FN}^* \end{bmatrix}^T + \begin{bmatrix} U_{Ad} & U_{Bd} & U_{Cd} & U_{Dd} & U_{Ed} & U_{Fd} \end{bmatrix}^T \quad (21)$$

where  $U_{Ad}$ ,  $U_{Bd}$ ,  $U_{Cd}$ ,  $U_{Dd}$ ,  $U_{Ed}$ , and  $U_{Fd}$  are the feedforward voltage compensations of phases A, B, C, D, E, and F, respectively.

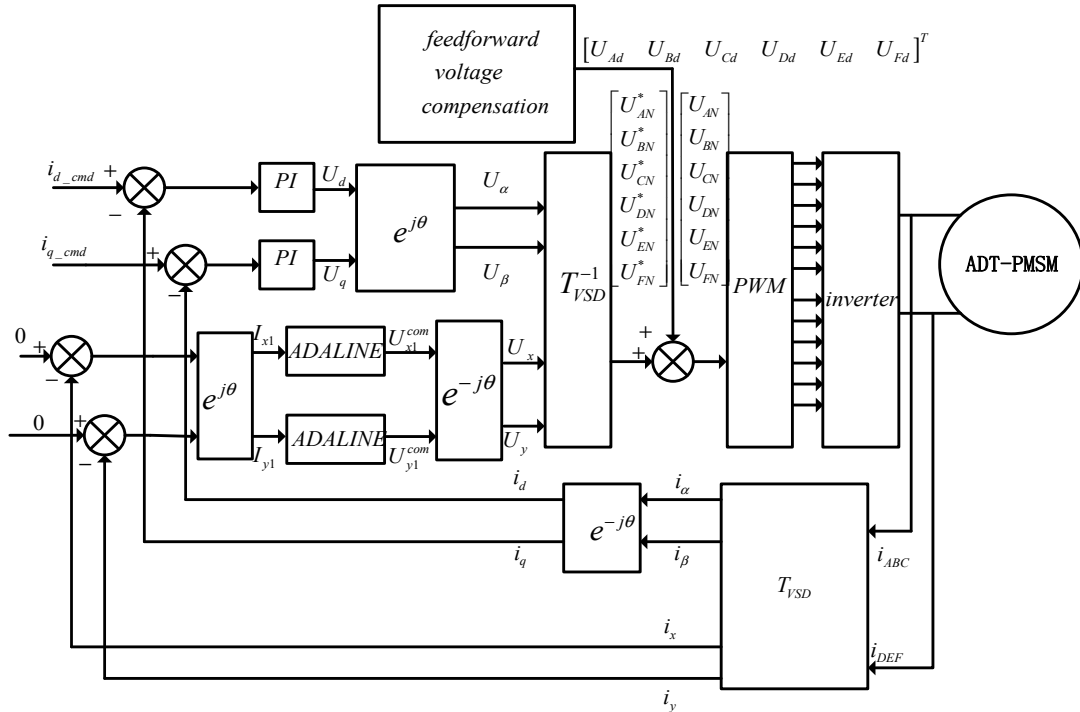


**Figure 10.** Diagram of control algorithm for asymmetric dual three-phase permanent magnet synchronous motor (ADT-PMSM).

Due to the isolated neutral points of ADT-PMSM, the three-phase zero-sequence voltage injection PWM technique can be adopted. The output PWM waveform is modulated by comparing the final reference voltage waveform of each phase with the triangular carrier waveform, which is also known as the carrier-based pulse width modulation (CBPWM). There are many methods for calculating zero-sequence components. Different zero-sequence components are corresponding to different PWM strategies [32]. In this paper, the commonly used mean zero sequence component injection, i.e., half of the middle value of the three-phase voltage values is used, as shown in Equation (22).

$$\begin{cases} U_{01} = -0.5(U_{\max 1} + U_{\min 1}) = 0.5U_{mid1} \\ U_{02} = -0.5(U_{\max 2} + U_{\min 2}) = 0.5U_{mid2} \end{cases} \quad (22)$$

where  $U_{\max}$ ,  $U_{mid}$  and  $U_{\min}$  are the maximum, middle, and the minimum values of the three-phase voltages.

Since the sum of three-phase voltages is zero, the zero-sequence voltage is equal to the half of the middle value of three-phase voltage values. It has been proved that the zero sequence voltage injection method is equivalent to the space vector pulse width modulation (SVPWM) algorithm, which can achieve the same linear voltage modulation range as proved in [14,15,32]. Compared to the four vector SVPWM algorithm, a four-dimension current control for ADT-PMSM can be implemented. Besides, it is easy to implement and the PWM waveform is centrally symmetrical and each power device is switched only once in each PWM cycle. Besides, it will not introduce even harmonics and can reduce switching losses. Figure 11 shows the double zero-sequence injection pulse width modulation (PWM) strategy.

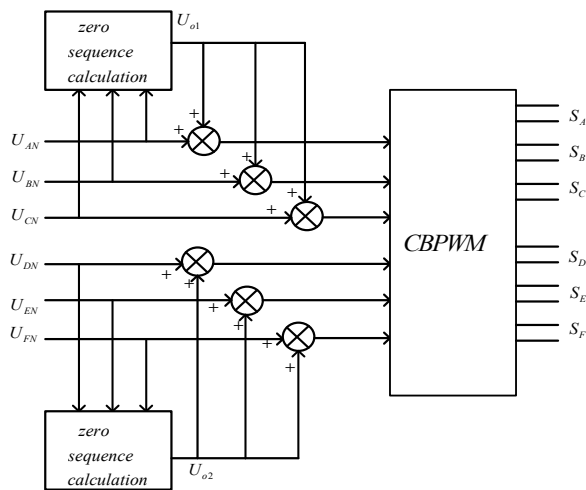


**Figure 11.** Double zero-sequence injection pulse width modulation (PWM) strategy.

## 6. Experimental Verification

The effectiveness of the proposed current harmonic suppression algorithm is verified by the implementation in an ADT-PMSM experimental platform (Siemens, Munich, Germany). The experimental setup is shown in Figure 12, which is composed of a DC machine mechanically coupled to the ADT-PMSM acting as a loading motor. The loading motor is controlled in speed control mode. The ADT-PMSM is supplied by using a two-level VSI (Infineon, Munich, Germany) configured for six-phase operation. A DC power supply is used to provide the DC-link voltage of 12V to the VSI. The complete control algorithm is implemented in a control board using Infineon TC277 (Infineon, Munich, Germany, 2017). The switching frequency is 10 kHz with 1  $\mu$ s of dead time provided by the hardware in the VSI (Infineon, Munich, Germany, 2017). To provide the current display at higher resolution, a current probe (CP150, Lecroy, New York, America, 2013) and Teledyne Lecroy oscilloscope (WaveSurfer 3024, Lecroy, New York, America, 2016) are used. The data of the phase currents are saved as Excel files with the help of an oscilloscope.

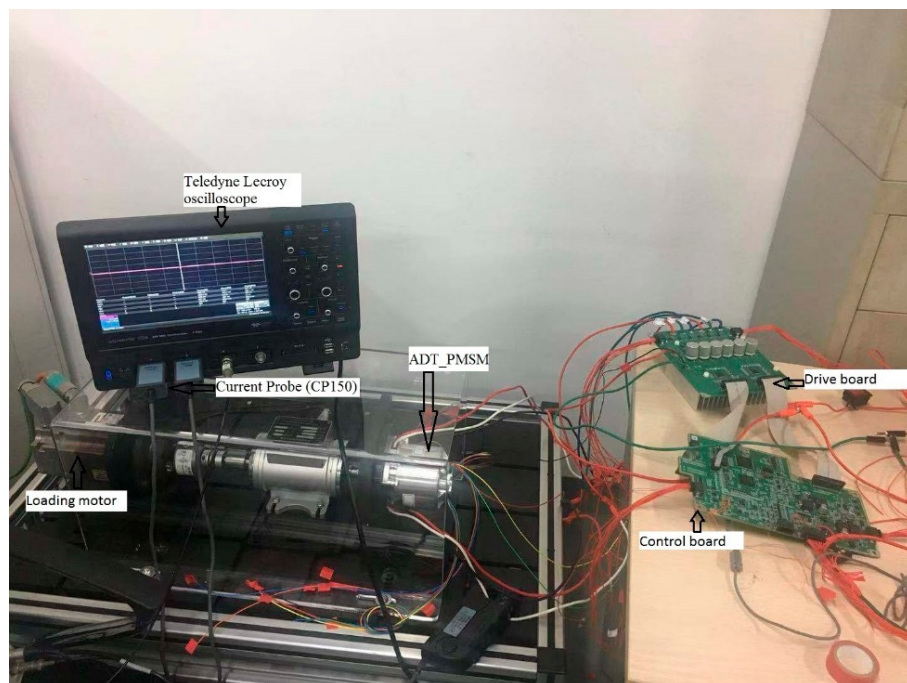


**Figure 12.** Experimental platform for ADT-PMSM.

The parameters for ADT-PMSM are given in Table 1, and the specifications of VSI are given in Table 2.

**Table 1.** Machine parameters.

Parameter, Unit	Value
Inductance value $d$ , H	$8 \times 10^{-5}$
Inductance value $q$ , H	$8 \times 10^{-5}$
Leakage inductance value, H	$7.2 \times 10^{-5}$
Flux, Wb	$5 \times 10^{-3}$
Pole pairs	4
Resistance, $\Omega$	$1.13 \times 10^{-2}$
Rated torque, N*m	$3 \pm 2.5\%$
Rated speed, rpm	1860
Rated phase current, A	50
Rated power, W	500

**Table 2.** Specifications of voltage source inverters (VSI).

Parameter, Unit	Value
DC-link voltage, V	12
Turn-on delay, ns	10
Turn-off delay, ns	22
Saturation vol. V	0.95
Diode forward vol. V	0.9
Dead time, $\mu$ s	1

Four cases are listed below to compare the performances.

Case 1: The algorithm is implemented without feedforward voltage compensation and a resonant controller;

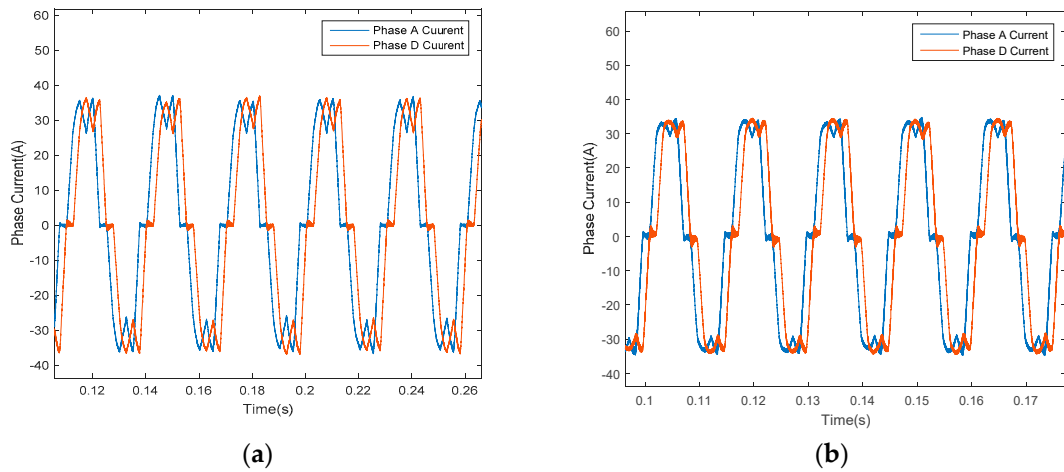
Case 2: The algorithm is implemented with feedforward voltage compensation only;

Case 3: The algorithm is implemented with resonant controller only;

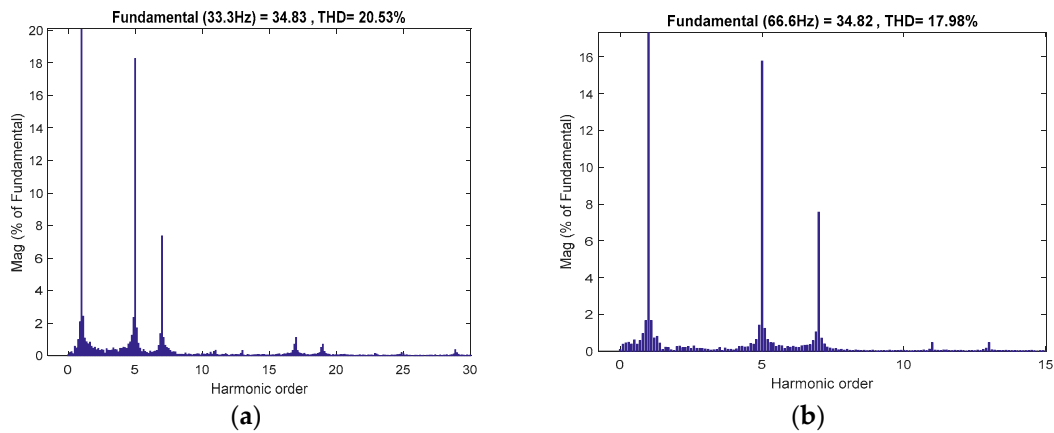
Case 4: The algorithm is implemented with both feedforward voltage compensation and a resonant controller.

Figure 13 shows the experimental results without employing feedforward voltage compensation and a resonant controller, which is equivalent to Case 1. Here, the command currents  $i_d$  and  $i_q$  are set to be 0 A and 35 A, respectively. The ADT-PMSM is operating under a current control loop and the speed is maintained at 500 rpm and 1000 rpm by the loading motor, respectively. Without the current closed-loop control strategy in the  $x$ - $y$  subspace and feedforward voltage compensation method,  $u_x$  and  $u_y$  are set to be 0 in order to avoid injecting extra harmonic voltages. It is obvious that the phase currents are severely distorted due to the dead-time effects and some other factors. A fast Fourier transform is conducted on the phase A current waveform as illustrated in Figure 14. From the figure, one can see that the phase current contains dominant fifth and seventh current harmonics and the total harmonic distortions (THD) are 20.53% and 17.98% respectively. Besides, it can be seen that the system is more sensitively influenced by the error voltage at low speed than at high speed, because the voltage error caused by dead time accounts for a large proportion at low speed.

Figure 15 depicts the experimental results after adopting the proposed feedforward voltage compensation which is equivalent to Case 2. The compensating voltages are calculated based on Equations (4), (5), and (6). The reference voltages are synthesized based on the proposed SVPWM method illustrated in Section 5. The waveforms of the phase currents have been improved a lot. The fifth and seventh current harmonics are significantly reduced. The THDs of the phase A current are reduced to 4.60% and 4.11% respectively with the proposed feedforward voltage compensation method, as shown in Figure 16.



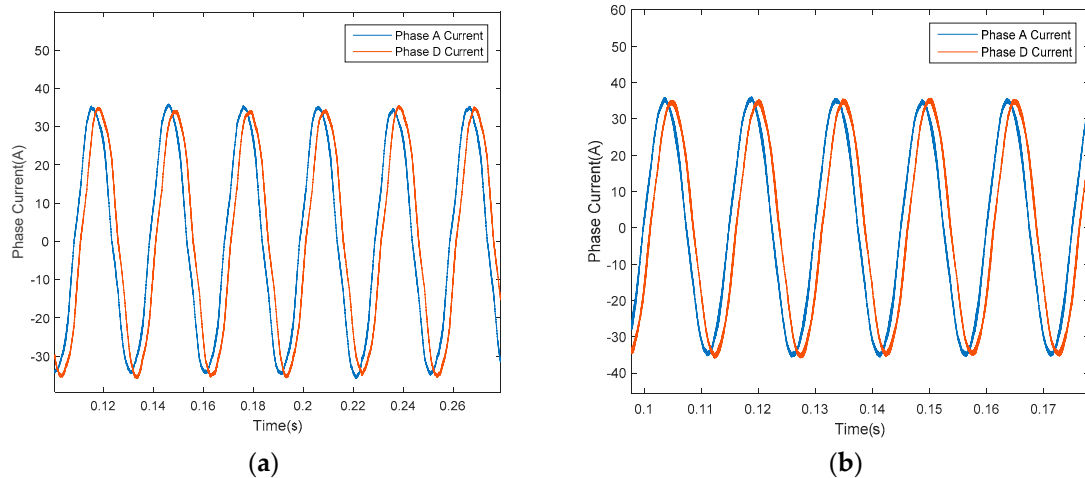
**Figure 13.** Phase A and D currents without adopting voltage compensation and resonant controller in the  $x$ - $y$  subspace, (a) speed is maintained at 500 rpm and (b) speed is maintained at 1000 rpm.



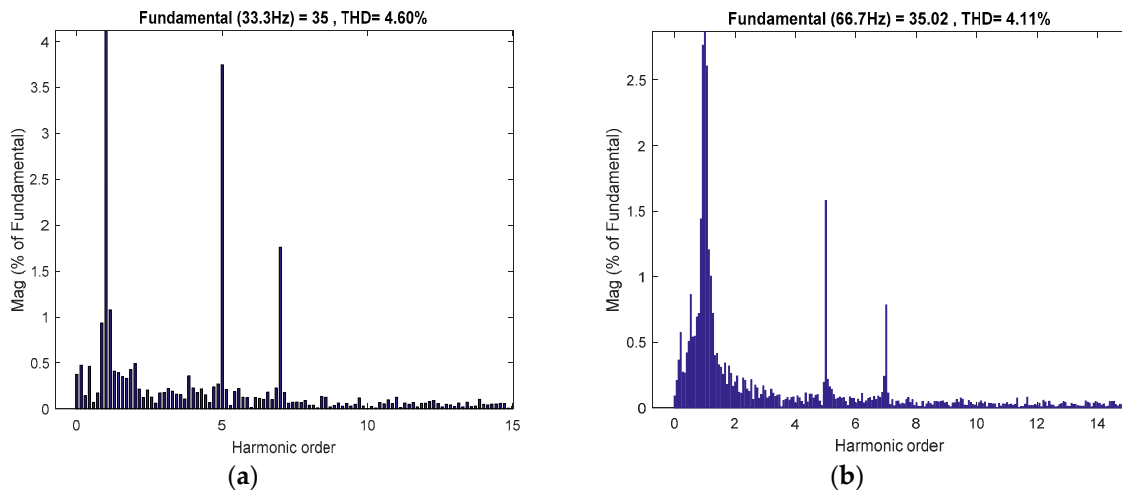
**Figure 14.** Total harmonic distortions (THDs) of the phase A current without adopting voltage compensation and resonant controller in  $x$ - $y$  subspace, (a) speed is maintained at 500 rpm and (b) speed is maintained at 1000 rpm.

Figure 17 shows the experimental results after adopting the proposed resonant controller, which is equivalent to Case 3. The reference voltages are synthesized based on the proposed SVPWM method, as illustrated in Section 5. The waveforms of phase currents have been improved. The fifth and seventh current harmonics are significantly reduced. The THDs of the phase A current value are reduced to 3.52% and 3.25% respectively with the proposed resonant controller, as shown in Figure 18.

Figure 19 depicts the experimental results after adopting both the proposed feedforward voltage compensation and resonant controller, which is equivalent to Case 4. The reference voltages are synthesized based on the proposed SVPWM method illustrated in Section 5. The waveforms of phase currents have been improved a lot, while the fifth and seventh current harmonics are significantly reduced. The THDs of the phase A current are reduced to 2.97% and 2.65% respectively with the proposed combination method, as shown in Figure 20. The THDs are the smallest among the four above-mentioned cases.



**Figure 15.** Phase A and D currents after adopting the proposed feedforward voltage compensation method only, (a) speed is maintained at 500 rpm, and (b) speed is maintained at 1000 rpm.



**Figure 16.** THDs of the phase A current after adopting the proposed feedforward voltage compensation method only, (a) speed is maintained at 500 rpm, and (b) speed is maintained at 1000 rpm.

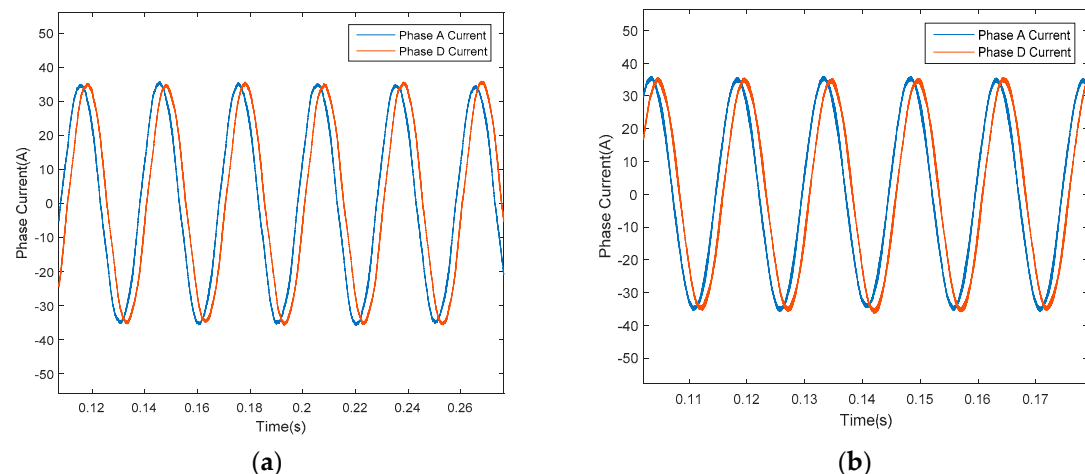


**Figure 17.** Phase A and D currents after adopting the proposed resonant controller only, (a) speed is maintained at 500 rpm, and (b) speed is maintained at 1000 rpm.

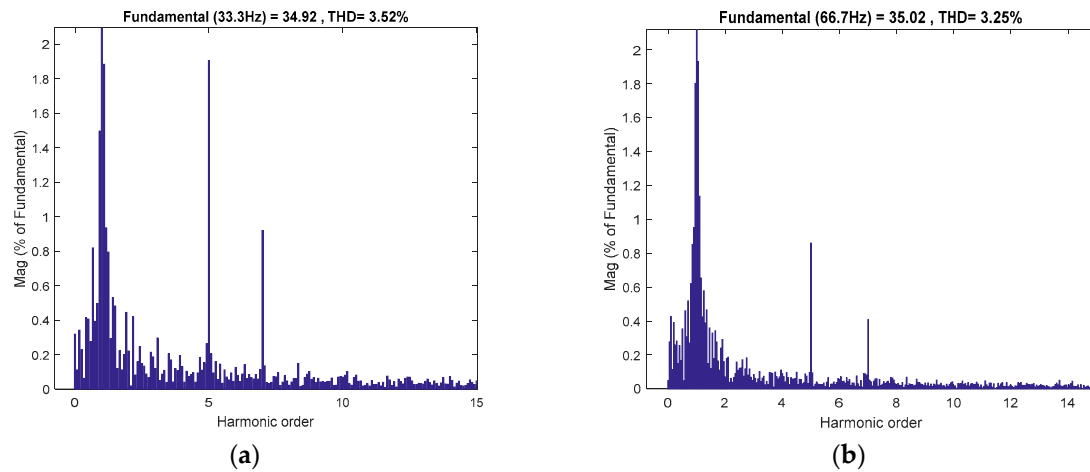


**Figure 18.** THDs of the phase A current after adopting the proposed resonant controller only, (a) speed is maintained at 500 rpm, and (b) speed is maintained at 1000 rpm.

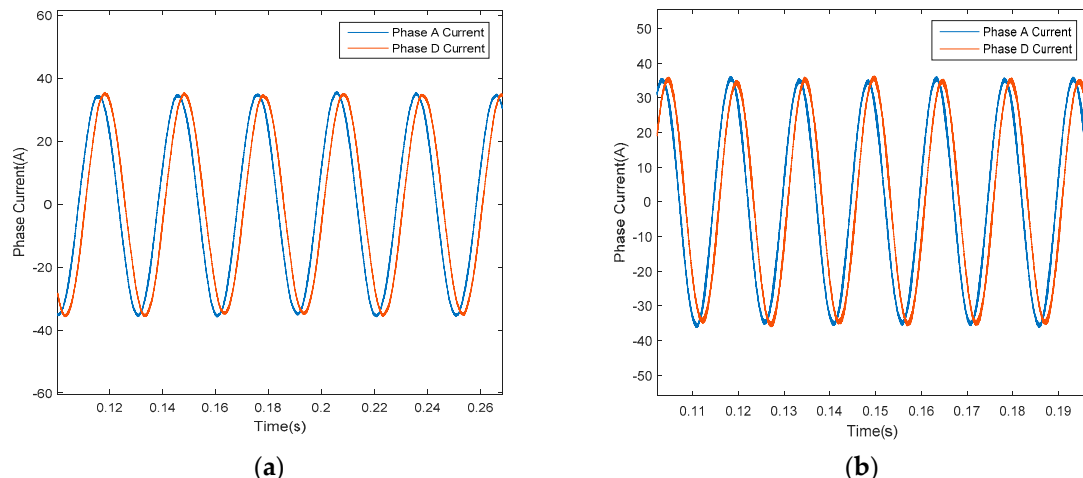


**Figure 19.** Phase A and D currents after adopting both feedforward voltage compensation and a resonant controller, (a) speed is maintained at 500 rpm, and (b) speed is maintained at 1000 rpm.

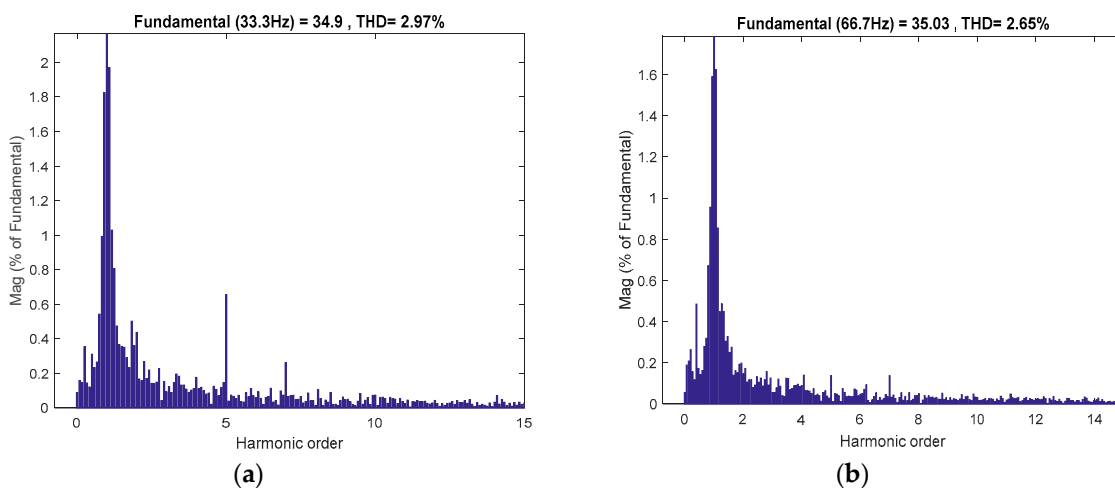


**Figure 20.** THDs of the phase A current after adopting both feedforward voltage compensation and a resonant controller, (a) speed is maintained at 500 rpm and (b) speed is maintained at 1000 rpm.

In order to facilitate the analysis, Table 3 shows the comparison of the THDs for four different cases under 500 rpm where the phase currents are 20 A and 35 A, respectively. The switching frequency is 10 kHz with 1  $\mu$ s of dead time. It can be seen that the THD when the phase current is 35 A is smaller than the THD when the phase current is 20 A, because the fundamental component is smaller when the phase current is 20 A. Besides, it is apparent that although the methods adopted for Case 2 and Case 3 can suppress the current harmonics effectively, the scheme for Case 4 is even more superior to the methods adopted for Case 2 and Case 3.

**Table 3.** Comparison of THDs under 500 rpm for four different cases.

Cases	Phase Current 20 A	Phase Current 35 A
Case 1	23.62%	20.53%
Case 2	5.82%	4.60%
Case 3	4.91%	3.52%
Case 4	3.68%	2.97%

Table 4 depicts the comparison of THD values for four different cases under 1000 rpm and phase currents are 20 A and 35 A, respectively. The switching frequency is 10 kHz with 1  $\mu$ s of dead time. It can be seen that as the speed increases, the system is more sensitively influenced by the error voltage at low speed than at high speed, because the voltage error caused by dead time accounts for a large proportion at low speed. We can obtain the conclusion that feedforward voltage compensation and the feedback current control loop in the  $x$ - $y$  subspace can suppress the current harmonics effectively, and employing both methods at the same time can achieve even better results.

**Table 4.** Comparison of THDs under 1000 rpm for four different cases.

Cases	Phase Current 20 A	Phase Current 35 A
Case 1	19.91%	17.98%
Case 2	5.23%	4.11%
Case 3	4.53%	3.25%
Case 4	3.12%	2.65%

## 7. Conclusions

Through the analysis of dead-time effects, this paper proposes a current harmonic suppression algorithm that combines the feedforward voltage compensation with a resonant controller implemented in the  $x$ - $y$  subspace as the feedback current controller. The feedforward voltage compensation can eliminate the current harmonics between 73% and 78% of its original value based on the accurate phase current polarities, which are determined based on the relationship between the current vector angle and the polarities. An improved resonant controller adopted in the  $x$ - $y$  subspace as the feedback current controller can suppress the current harmonics between 76% and 84% in the  $x$ - $y$  subspace. The experimental results verify that not only the feedforward voltage compensation but also the improved resonant controller employed in the  $x$ - $y$  subspace can suppress the current harmonics effectively. Meanwhile, employing both methods at the same time can eliminate the current harmonics between 84% and 86%, which can achieve even better results compared to the cases of adopting only one method.

**Author Contributions:** Conceptualization, Z.W., Y.Z. and W.G.; methodology, Z.W., Y.Z. and W.G.; software, Z.W., Y.Z., and K.L.; validation, Z.W., Y.Z., W.G., K.L., and J.G.; formal analysis, Z.W.; investigation, W.G. and K.L.; resources, Z.W., Y.Z., W.G., K.L., and J.G.; data curation, Z.W., Y.Z., W.G., K.L., and J.G.; writing—original draft preparation, Z.W., Y.Z., W.G., K.L., and J.G.; writing—review and editing, Z.W., Y.Z., W.G., K.L., and J.G.; visualization, Z.W., Y.Z., W.G., K.L., and J.G.; supervision, Z.W.; project administration, Y.Z.; funding acquisition, Z.W., Y.Z., and K.L. All authors have read and agreed to the published version of the manuscript.

**Funding:** This research is supported by National Key Research and Development Program of China (2016YFB0100804).

**Conflicts of Interest:** The authors declare no conflicts of interests.

## References

1. Zheng, J.; Huang, S.; Rong, F.; Lye, M. Six-Phase Space Vector PWM under Stator One-Phase Open-Circuit Fault Condition. *Energies* **2018**, *11*, 1796. [[CrossRef](#)]
2. Shi, L.; An, J.; Zhang, W. Topology Comparison Study of Five-Phase Wound-Field Doubly Salient Fault Tolerant Generators. *Appl. Sci.* **2019**, *9*, 2112. [[CrossRef](#)]
3. Mohammadpour, A.; Parsa, L. Global Fault-Tolerant Control Technique for Multiphase Permanent-Magnet Machines. *IEEE Trans. Ind. Appl.* **2015**, *51*, 178–186. [[CrossRef](#)]
4. de Lillo, L.; Empringham, L.; Wheeler, P.W.; Khwan-On, S.; Gerada, C.; Othman, M.N.; Huang, X. Multiphase Power Converter Drive for Fault-Tolerant Machine Development in Aerospace Applications. *IEEE Trans. Ind. Electron.* **2010**, *57*, 575–583. [[CrossRef](#)]
5. Geng, Y.; Lai, Z.; Li, Y.; Wang, D.; Chen, R.; Zheng, P. Sensorless Fault-Tolerant Control Strategy of Six-Phase Induction Machine Based on Harmonic Suppression and Sliding Mode Observer. *IEEE Access* **2019**, *7*, 110086–110102. [[CrossRef](#)]
6. Patkar, F.; Jones, M. Performance of an asymmetrical six-phase induction machine in single-and two-neutral point configurations. In Proceedings of the 2013 48th International Universities' Power Engineering Conference (UPEC), Dublin, Ireland, 2–5 September 2013.
7. Wu, Z.; Gu, W.; Zhu, Y.; Lu, K. Current Control Methods for an Asymmetric Six-Phase Permanent Magnet Synchronous Motor. *Electronics* **2020**, *9*, 172. [[CrossRef](#)]
8. Bojoi, R.; Profumo, F.; Tenconi, A. Digital synchronous frame current regulation for dual three-phase induction motor drives. In Proceedings of the IEEE 34th Annual Conference on Power Electronics Specialist, Acapulco, Mexico, 15–19 June 2003.
9. Zhao, Y.; Lipo, T.A. Space vector PWM control of dual three-phase induction machine using vector space decomposition. *IEEE Trans. Ind. Appl.* **1995**, *31*, 1100–1109. [[CrossRef](#)]
10. Prieto, J.; Barrero, F.; Jones, M.; Levi, E. A modified continuous PWM technique for asymmetrical six-phase induction machines. In Proceedings of the 2010 IEEE International Conference on Industrial Technology, Vina del Mar, Chile, 14–17 March 2010.
11. Che, H.S.; Hew, W.P.; Rahim, N.A.; Levi, E.; Jones, M.; Duran, M.J. Current Control of a Six-Phase Induction Generator for Wind Energy Plants. In Proceedings of the 2012 15th International Power Electronics and Motion Control Conference (EPE/PEMC), Novi Sad, Serbia, 4–6 September 2012.
12. Ahmad, M.; Wang, Z.; Yan, S.; Wang, C.; Wang, Z.; Zhu, C.; Qin, H. Comparative Analysis of Two and Four Current Loops for Vector Controlled Dual-Three Phase Permanent Magnet Synchronous Motor. *Electronics* **2018**, *7*, 269. [[CrossRef](#)]
13. Che, H.S.; Levi, E.; Jones, M.; Hew, W.; Rahim, N.A. Current Control Methods for an Asymmetrical Six-Phase Induction Motor Drive. *IEEE Trans. Power Electron.* **2014**, *29*, 407–417. [[CrossRef](#)]
14. Hadiouche, D.; Baghli, L.; Rezzoug, A. Space-vector PWM techniques for dual three-phase AC machine: Analysis, performance evaluation, and DSP implementation. *IEEE Trans. Ind. Appl.* **2006**, *4*, 1112–1122. [[CrossRef](#)]
15. Marouani, K.; Baghli, L.; Hadiouche, D.; Kheloui, A.; Rezzoug, A. A New PWM Strategy Based on a 24-Sector Vector Space Decomposition for a Six-Phase VSI-Fed Dual Stator Induction Motor. *IEEE Trans. Ind. Electron.* **2008**, *55*, 1910–1920. [[CrossRef](#)]
16. Yuan, L.; Chen, M.; Shen, J.; Xiao, F. Current harmonics elimination control method for six-phase PM synchronous motor drives. *ISA Trans.* **2015**, *59*, 443–449. [[CrossRef](#)] [[PubMed](#)]
17. Ruan, Z.; Song, W.; Yan, Y. Current Harmonic Suppression for Dual Three-Phase Permanent Magnet Synchronous Motor Drives. *IEEE Access* **2019**, *7*, 143888–143898. [[CrossRef](#)]
18. Zhang, H.; Kou, B.; Zhang, L.; Zhang, H. Analysis and Compensation of Dead-Time Effect of a ZVT PWM Inverter Considering the Rise- and Fall-Times. *Appl. Sci.* **2016**, *6*, 344. [[CrossRef](#)]
19. Choi, J.-W.; Sul, S.-K. Inverter output voltage synthesis using novel dead time compensation. *IEEE Trans. Power Electron.* **1996**, *11*, 221–227. [[CrossRef](#)]
20. Kerkman, R.J.; Leggate, D.; Schlegel, D.W.; Winterhalter, C. Effects of parasitics on the control of voltage source inverters. *IEEE Trans. Power Electron.* **2003**, *18*, 140–150. [[CrossRef](#)]

21. Munoz, A.R.; Lipo, T.A. On-line dead-time compensation technique for open-loop PWM-VSI drives. *IEEE Trans. Power Electron.* **1999**, *14*, 683–689. [[CrossRef](#)]
22. Lin, Y.; Lai, Y. Dead-Time Elimination of PWM-Controlled Inverter/Converter Without Separate Power Sources for Current Polarity Detection Circuit. *IEEE Trans. Ind. Electron.* **2009**, *56*, 2121–2127.
23. Xia, C.; Ji, B.; Yan, Y. Smooth Speed Control for Low-Speed High-Torque Permanent-Magnet Synchronous Motor Using Proportional–Integral–Resonant Controller. *IEEE Trans. Ind. Electron.* **2015**, *62*, 2123–2134. [[CrossRef](#)]
24. Yepes, A.G.; Freijedo, F.D.; Lopez, Ó.; Doval-Gandoy, J. High-Performance Digital Resonant Controllers Implemented with Two Integrators. *IEEE Trans. Power Electron.* **2011**, *26*, 563–576. [[CrossRef](#)]
25. Shi, W.; Lin, F.; Yang, Z. A new method based on PIR controller to reject torque and current ripple under fluctuating DC voltage for high-speed train traction drives. In Proceedings of the 2012 15th International Conference on Electrical Machines and Systems (ICEMS), Sapporo, Japan, 21–24 October 2012.
26. Yepes, A.G.; Malvar, J.; Vidal, A.; López, O.; Doval-Gandoy, J. Current Harmonics Compensation Based on Multiresonant Control in Synchronous Frames for Symmetrical  $n$ -Phase Machines. *IEEE Trans. Ind. Electron.* **2015**, *62*, 2708–2720. [[CrossRef](#)]
27. Hwang, S.; Kim, J. Dead Time Compensation Method for Voltage-Fed PWM Inverter. *IEEE Trans. Energy Convers.* **2010**, *25*, 1–10. [[CrossRef](#)]
28. Urasaki, N.; Senju, T.; Uezato, K.; Funabashi, T. On-line dead-time compensation method for permanent magnet synchronous motor drive. In Proceedings of the 2002 IEEE International Conference on Industrial Technology, Bangkok, Thailand, 11–14 December 2002.
29. Kim, H.-S.; Moon, H.-T.; Youn, M.-J. On-line dead-time compensation method using disturbance observer. *IEEE Trans. Power Electron.* **2003**, *18*, 1336–1345.
30. Urasaki, N.; Senju, T.; Uezato, K.; Funabashi, T. Adaptive Dead-Time Compensation Strategy for Permanent Magnet Synchronous Motor Drive. *IEEE Trans. Energy Convers.* **2007**, *22*, 271–280. [[CrossRef](#)]
31. Park, D.; Kim, K. Parameter-Independent Online Compensation Scheme for Dead Time and Inverter Nonlinearity in IPMSM Drive Through Waveform Analysis. *IEEE Trans. Ind. Electron.* **2014**, *61*, 701–707. [[CrossRef](#)]
32. Zhou, K.; Wang, D. Relationship between space-vector modulation and three-phase carrier-based PWM: A comprehensive analysis [three-phase inverters]. *IEEE Trans. Ind. Electron.* **2002**, *49*, 186–196. [[CrossRef](#)]



© 2020 by the authors. Licensee MDPI, Basel, Switzerland. This article is an open access article distributed under the terms and conditions of the Creative Commons Attribution (CC BY) license (<http://creativecommons.org/licenses/by/4.0/>).